Sensors and Materials, Vol. 37, No. 12 (2025) 5487–5499
MYU Tokyo

S & M 4258

Speed Estimation Field-orientation-controlled Interior Permanent Magnet Synchronous Motor Drive Using High-frequency Signal Injection Technique

Yung-Chang Luo,* Hao-You Huang, Hong-Wei Sian, and Chih-Liang Chung

Department of Electrical Engineering, National Chin-Yi University of Technology,
No. 57, Sec. 2, Zhongshan Rd, Taiping Dist, Taichung 41170, Taiwan (ROC)

(Received April 30, 2025; accepted November 26, 2025)

Keywords: field orientation control (FOC), interior permanent magnet synchronous motor (IPMSM) drive, speed estimation, high-frequency signal injection, rotor position estimation

A high-frequency signal injection technique was proposed for speed estimation in a field-orientation-controlled (FOC) interior permanent magnet synchronous motor (IPMSM) drive. The decoupled FOC IPMSM drive based on the stator current and flux was established to achieve a maximum torque-to-current ratio, with stator current measurements obtained using Hall effect current sensors. On the basis of the linear control of the two-axis stator current and speed loops, a systematic controller parameter design was developed by the pole placement method. A high-frequency voltage signal was injected into the IPMSM, and the resulting high-frequency current response was utilized to estimate the rotor position. The estimated rotor position was then employed to enable the speed estimation of the FOC IPMSM drive. The MATLAB®\Simulink toolbox was used to establish this simulation system, and all the control algorithms were realized with a TI 6713 digital signal processor and an F2812 microcontroller card to validate the proposed approach. Both simulation and experimental results confirmed the effectiveness of the proposed method.

1. Introduction

Interior permanent magnet synchronous motors (IPMSMs) are widely used in energy-saving automation industries owing to their robustness, reliability, superior torque capacity, high efficiency, and low maintenance requirements. The mathematical model of an IPMSM is complex; however, by applying the field-orientation-controlled (FOC) method—similar to that of a separately excited DC motor—the torque and flux can be controlled independently. According to FOC theory,[1] through coordinate transformation, the IPMSM mathematical model is separated into torque-current and flux-current components. Since torque and flux are orthogonal to each other, the maximum torque-to-current ratio is achieved. The implementation of a conventional FOC IPMSM drive typically requires an encoder or a resolver to detect the shaft position. However, the use of such sensors reduces the drive robustness and limits

*Corresponding author: e-mail: luoyc@ncut.edu.tw
https://doi.org/10.18494/SAM5718

ISSN 0914-4935
https://myukk.org/

applicability in harsh environments. Several speed detection methods for IPMSM drives have been proposed, including speed estimation based on back electromotive force (EMF),[2–6] observer- or flux estimator-based speed determination,[7–10] speed adjustment using fuzzy logic control or neural networks,[11–14] and speed estimation derived from adaptive control theory or Kalman filters.[15–19] In this study, a decoupled FOC IPMSM drive based on stator current and flux was developed, with electromagnetic Hall effect current sensors used to measure the three-phase stator currents of the IPMSM. With the linear control of the two-axis stator current and speed loops, a systematic controller parameter design was proposed by the pole placement method. A high-frequency voltage signal was injected into the IPMSM, and the resulting high-frequency current response was utilized to estimate the rotor position, enabling the speed estimation of the FOC IPMSM drive.

This paper is organized into six sections. In Sect. 1, we present the research background, motivation, and a review of speed estimation methods for FOC IPMSM drives. In Sect. 2, we describe the development of the decoupled FOC IPMSM drive system. The systematic controller parameter design based on pole placement for the two-axis stator current and speed loops is detailed in Sect. 3. In Sect. 4, we explain the speed estimation method using a high-frequency signal injection technique. In Sects. 5 and 6, we discuss the simulation and experimental results, and present our conclusions, respectively.

2. Decoupled FOC IPMSM Drive System

The stator voltage equation of an IPMSM in the three-phase reference frame is given by[20]

$$\vec{v}_s = R_s \vec{i}_s + p\vec{\lambda}_s , \tag{1}$$

where $\vec{v}_s$, $\vec{i}_s$, and $\vec{\lambda}_s$ are the stator voltage, current, and flux, respectively, R_s is the stator resistance, and $p = d/dt$ is the differential operator.

The coordinate transformation from the three-phase reference frame to the two-axis synchronous reference frame is given as

$$\vec{v}_s = (1/c)\vec{v}_s^{\,e} e^{j\theta_e}, \quad \vec{i}_s = (1/c)\vec{i}_s^{\,e} e^{j\theta_e}, \quad \vec{\lambda}_s = (1/c)\vec{\lambda}_s^{\,e} e^{j\theta_e}, \tag{2}$$

where j represents the imaginary part; $\vec{v}_s^{\,e} = v_{ds}^e + jv_{qs}^e$, $\vec{i}_s^{\,e} = i_{ds}^e + ji_{qs}^e$, and $\vec{\lambda}_s^{\,e} = \lambda_{ds}^e + j\lambda_{qs}^e$ denote the stator voltage, current, and flux in the two-axis synchronous reference frame, respectively; $e^{j\theta_e}$ represents the polar angle; θ_e is the position of the synchronous reference frame; and c = 1/3 is the coordinate transformation constant.

On the basis of Eq. (2), the d^e-axis and q^e-axis stator voltage equations in the synchronous reference frame are derived as

$$v_{ds}^e = R_s i_{ds}^e + p\lambda_{ds}^e - \omega_e \lambda_{qs}^e , \tag{3}$$

$$v_{qs}^{e} = R_s i_{qs}^{e} + p\lambda_{qs}^{e} + \omega_e \lambda_{ds}^{e}, \tag{4}$$

where ω_e is the speed of the synchronous reference frame.

The d^e-axis of an IPMSM is aligned with the stator winding axis, whereas the q^e-axis is aligned with the stator core axis. The air gap along the q^e-axis is larger than that along the d^e-axis, resulting in a higher magnetic reluctance along the q^e-axis than along the d^e-axis. Since inductance is inversely proportional to magnetic reluctance, this difference leads to

$$L_d > L_q, \tag{5}$$

where L_d and L_q are the d^e-axis and q^e-axis stator inductances, respectively.

Since the rotor permanent magnets are located only along the d^e-axis, the stator fluxes along the d^e- and q^e-axes are expressed as

$$\lambda_{ds}^{e} = L_d i_{ds}^{e} + \lambda_{rF}, \tag{6}$$

$$\lambda_{qs}^{e} = L_q i_{qs}^{e}, \tag{7}$$

where λ_{rF} is the equivalent flux of the rotor permanent magnets linked to the stator. By substituting Eqs. (6) and (7) into Eqs. (3) and (4), the d^e-axis and q^e-axis stator current state equations are derived as

$$p\begin{bmatrix} i_{ds}^{e} \\ i_{qs}^{e} \end{bmatrix} = \begin{bmatrix} -R_s/L_d & (L_q/L_d)\omega_e \\ -(L_d/L_q)\omega_e & -R_s/L_q \end{bmatrix}\begin{bmatrix} i_{ds}^{e} \\ i_{qs}^{e} \end{bmatrix} + \begin{bmatrix} (1/L_d)v_{ds}^{e} \\ (1/L_q)v_{qs}^{e} - (1/L_q)\omega_e\lambda_{rF} \end{bmatrix}. \tag{8}$$

Examining the first row of Eq. (8) reveals that the second term on the right side is a coupling component associated with the q^e-axis stator current. Furthermore, examining the second row of Eq. (8) shows that the first and fourth terms on the right side are the coupling components related to the d^e-axis stator current and rotor equivalent flux, respectively. Using these coupling components, the feedforward compensations for the d^e-axis and q^e-axis stator voltages are defined as

$$\begin{bmatrix} v_{ds\_fc}^{e} \\ v_{qs\_fc}^{e} \end{bmatrix} = \begin{bmatrix} -(L_q/L_d)\omega_e i_{qs}^{e} \\ (L_d/L_q)\omega_e i_{ds}^{e} + (1/L_q)\omega_e\lambda_{rF} \end{bmatrix}. \tag{9}$$

The realization of linear control for the d^e-axis and q^e-axis stator current loops is achieved by

$$p\begin{bmatrix} i_{ds}^{e} \\ i_{qs}^{e} \end{bmatrix} = \begin{bmatrix} -R_s/L_d & 0 \\ 0 & -R_s/L_q \end{bmatrix}\begin{bmatrix} i_{ds}^{e} \\ i_{qs}^{e} \end{bmatrix} + \begin{bmatrix} (1/L_d)v_{ds}^{e'} \\ (1/L_q)v_{qs}^{e'} \end{bmatrix}, \tag{10}$$

where $v_{ds}^{e'}$ and $v_{qs}^{e'}$ are the outputs of the d^e-axis and q^e-axis stator current controllers, respectively. The voltage commands for the d^e-axis and q^e-axis stator current control loops are expressed as

$$\begin{bmatrix} v_{ds}^{e^*} \\ v_{qs}^{e^*} \end{bmatrix} = \begin{bmatrix} (1/L_d)v_{ds}^{e'} \\ (1/L_q)v_{qs}^{e'} \end{bmatrix} + \begin{bmatrix} v_{ds\_fc}^{e} \\ v_{qs\_fc}^{e} \end{bmatrix}, \tag{11}$$

where $v_{ds}^{e^*}$ and $v_{qs}^{e^*}$ are the voltage commands for the d^e-axis and q^e-axis stator current control loops, respectively. Using Eq. (10), the plant transfer functions of the d^e-axis and q^e-axis stator current control loops are derived as

$$\begin{bmatrix} G_{p\_d}(s) \\ G_{p\_q}(s) \end{bmatrix} \equiv \begin{bmatrix} i_{ds}^{e}/v_{ds}^{e'} \\ i_{qs}^{e}/v_{qs}^{e'} \end{bmatrix} = \begin{bmatrix} (1/L_d)/(s + R_s/L_d) \\ (1/L_q)/(s + R_s/L_q) \end{bmatrix}, \tag{12}$$

where $G_{p\_d}(s)$ and $G_{p\_q}(s)$ are the plant transfer functions of the d^e-axis and q^e-axis stator current control loops, respectively, and s is the Laplace operator.

The torque developed by the IPMSM is expressed as

$$T_e = (3P/4)(i_{qs}^{e}\lambda_{rF} + (L_d - L_q)i_{ds}^{e}i_{qs}^{e}), \tag{13}$$

where P is the number of IPMSM poles. In Eq. (13), the first term on the right side represents the electromagnetic torque and the second term corresponds to the reluctance torque. This reluctance torque is an additional torque component unique to the IPMSM, distinguishing it from surface-mounted permanent magnet synchronous motors (SPMSMs). Furthermore, i_{qs}^{e} and λ_{rF} are orthogonal, and the maximum torque-to-current ratio control is achieved. The mechanical equation of the IPMSM is given by

$$T_e = J_m p\omega_{rm} + B_m\omega_{rm} + T_L, \tag{14}$$

where J_m is the inertia of the IPMSM rotor, B_m is the viscous friction coefficient, T_L is the load torque, $\omega_{rm} = (2/P)\omega_r$ is the mechanical speed of the IPMSM rotor shaft, and ω_r is the electric speed of the rotor. The bandwidth of the inner stator current control loop is much higher than that of the outer speed control loop. Using Eq. (14), $\Delta T_e = T_e - T_L$ is defined, and then, the plant

transfer function of the speed control loop is obtained as

$$G_{p\_s}(s) \equiv \omega_{rm} / \Delta T_e = (1/J_m)/(s + B_m/J_m) . \tag{15}$$

Figure 1 illustrates the control block diagram of the decoupled FOC IPMSM drive. Here, (K_{ps}, K_{is}), (K_{pd}, K_{id}), and (K_{pq}, K_{iq}) represent the proportional and integral gain parameter pairs of the speed, d^e-axis stator current, and q^e-axis stator current controllers, respectively. The rotor flux is provided by the permanent magnets, and the d^e-axis stator current command is set as a value of 0.

3. Controller Parameter Design Using Pole Placement Method

A systematic controller parameter design using the pole placement method was proposed for the d^e-axis and q^e-axis stator current controllers as well as the speed controller. According to Eqs. (12) and (15), these three controllers are first-order systems, and the corresponding three proportional-and-integral–type (PI-type) controllers are also first-order, making it suitable to apply the pole placement method to determine the controller parameters. The transfer function of each plant is defined as

$$G_p(s) = K_a / (1 + s\tau) , \tag{16}$$

where K_a and τ are the gain and time constant of the plant, respectively. Furthermore, the transfer function of each PI-type controller is defined as

$$G_c(s) \equiv K_p + K_i / s = K_P (1 + (1/sT_c)) , \tag{17}$$

where $T_c = K_p / K_i$. On the basis of Eqs. (16) and (17), the closed-loop transfer function with unity feedback is obtained as

$$G_{cl}(s) = G_p(s) G_c(s) / (1 + G_p(s) G_c(s)) . \tag{18}$$

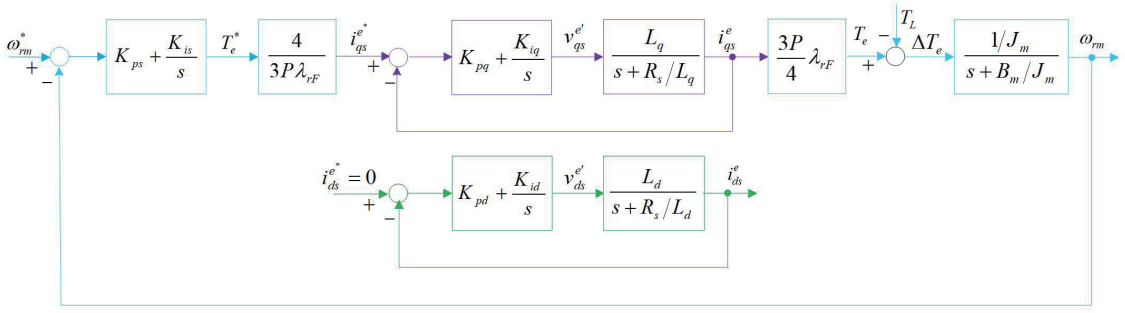

Fig. 1. (Color online) Decoupled linear control block diagram of the FOC IPMSM drive.

The characteristic equation corresponding to Eq. (18) is given by

$$1 + G_p(s)G_c(s) = 0 . \tag{19}$$

Equation (19) can be rewritten as

$$s^2 + ((1 + K_p K_a)/\tau)s + K_p K_a/(\tau T_c) = 0 . \tag{20}$$

The standard form of the characteristic equation for a second-order system is expressed as

$$s^2 + 2\varsigma\omega_0 s + \omega_0^2 = 0 . \tag{21}$$

The damping coefficient (ς) and natural frequency (ω_0) can be predetermined in accordance with the desired control performance requirements. By comparing Eqs. (20) and (21), the controller parameters K_p and K_i can be expressed as functions of ς and ω_0 as

$$K_p = (2\varsigma\omega_0\tau - 1)/K_a , \tag{22}$$

$$K_i = \tau\omega_0^2/K_a . \tag{23}$$

In this study, the parameters of the three PI-type controllers were designed on the basis of Eqs. (22) and (23). The proportional gain (K_p), integral gain (K_i), damping coefficient (ς), natural frequency (ω_0), and bandwidth (BW) of the three designed controllers are listed in Table 1.

4. Speed Estimation Method Based on High-frequency Signal Injection Technique

Speed estimation for the FOC IPMSM drive requires an estimated rotor speed signal to replace the feedback rotor speed used in conventional FOC IPMSM drives. In this study, a high-frequency signal injection technique is employed to design the estimated rotor speed signal.

When a high-frequency signal with a fixed frequency is injected into the IPMSM, and only the high-frequency components are considered, the back EMF and stator resistance voltage drop can be neglected. The high-frequency component of Eq. (8) can then be rewritten as[21]

Table 1
Controller parameters, performance requirements, and bandwidths.

	K_p	K_i	ς	ω_0	BW
d^e-axis stator current controller	6.349	7618.7	0.707	1951.615	2380
q^e-axis stator current controller	2.2138	2656.56	0.707	1994.041	2190
Speed controller	0.17392	12.1744	0.707	132.6523	183

$$\begin{bmatrix} j\omega_h L_{dh} & 0 \\ 0 & j\omega_h L_{qh} \end{bmatrix} \begin{bmatrix} i_{dsh}^e \\ i_{qsh}^e \end{bmatrix} = \begin{bmatrix} v_{dsh}^e \\ v_{qsh}^e \end{bmatrix}, \tag{24}$$

where ω_h represents the frequency of the high-frequency voltage signal; L_{dh} and L_{qh} are the high-frequency inductances along the d^e- and q^e-axes, respectively, when a high-frequency signal is applied; i_{dsh}^e and i_{qsh}^e are the high-frequency currents along the d^e- and q^e-axes, respectively; v_{dsh}^e and v_{qsh}^e are the high-frequency injected voltages along the d^e- and q^e-axes, respectively. The estimation error angle of the rotor can be expressed as

$$\tilde{\theta}_r = \theta_r - \hat{\theta}_r, \tag{25}$$

where $\tilde{\theta}_r$ is the estimation error angle of the rotor, θ_r is the actual rotor position angle, and $\hat{\theta}_r$ is the estimated rotor position angle.

The two-axis reference frame based on the actual rotor angle θ_r is defined as the $d^r - q^r$-axis frame, and the two-axis reference frame based on the estimated rotor angle $\hat{\theta}_r$ is defined as the $\hat{d}^r - \hat{q}^r$-axis frame. According to Eq. (25), the angular difference between the d^r-axis and the $\hat{d}^r$-axis is $\tilde{\theta}_r$. Thus, Eq. (24) can be transformed into the high-frequency voltage components expressed in the estimated reference frame considering the angular estimation error $\tilde{\theta}_r$ as

$$\begin{bmatrix} j\omega_h L_{dh} & 0 \\ 0 & j\omega_h L_{qh} \end{bmatrix} \begin{bmatrix} \cos\tilde{\theta}_r & \sin\tilde{\theta}_r \\ -\sin\tilde{\theta}_r & \cos\tilde{\theta}_r \end{bmatrix} \begin{bmatrix} i_{\tilde{d}sh}^e \\ i_{\tilde{q}sh}^e \end{bmatrix} = \begin{bmatrix} \cos\tilde{\theta}_r & \sin\tilde{\theta}_r \\ -\sin\tilde{\theta}_r & \cos\tilde{\theta}_r \end{bmatrix} \begin{bmatrix} v_{\tilde{d}sh}^e \\ v_{\tilde{q}sh}^e \end{bmatrix}, \tag{26}$$

where $i_{\tilde{d}sh}^e$ and $i_{\tilde{q}sh}^e$ are the high-frequency currents along the $\hat{d}^r$- and $\hat{q}^r$-axes, and $v_{\tilde{d}sh}^e$ and $v_{\tilde{q}sh}^e$ are the high-frequency voltages along the $\hat{d}^r$- and $\hat{q}^r$-axes, respectively. By defining $L_{avg} = (L_{dh} + L_{qh})/2$ and $L_{dif} = (L_{dh} - L_{qh})/2$, Eq. (26) can be further derived as[22]

$$\begin{bmatrix} j\omega_h (L_{avg} + L_{dif}\cos 2\tilde{\theta}_r) & j\omega_h L_{dif}\sin 2\tilde{\theta}_r \\ j\omega_h L_{dif}\sin 2\tilde{\theta}_r & j\omega_h (L_{avg} - L_{dif}\cos 2\tilde{\theta}_r) \end{bmatrix} \begin{bmatrix} i_{\tilde{d}sh}^e \\ i_{\tilde{q}sh}^e \end{bmatrix} = \begin{bmatrix} v_{\tilde{d}sh}^e \\ v_{\tilde{q}sh}^e \end{bmatrix}. \tag{27}$$

The high-frequency currents along the $\hat{d}^r$- and $\hat{q}^r$-axes can be derived from Eq. (27) as

$$\begin{bmatrix} i_{\tilde{d}sh}^e \\ i_{\tilde{q}sh}^e \end{bmatrix} = \frac{1}{(j\omega_h L_{dh})(j\omega_h L_{qh})} \begin{bmatrix} L_{avg} - L_{dif}(\cos 2\tilde{\theta}_r) & -L_{dif}(\sin 2\tilde{\theta}_r) \\ -L_{dif}(\sin 2\tilde{\theta}_r) & L_{avg} + L_{dif}(\cos 2\tilde{\theta}_r) \end{bmatrix} \begin{bmatrix} v_{\tilde{d}sh}^e \\ v_{\tilde{q}sh}^e \end{bmatrix}. \tag{28}$$

To reduce the torque ripple generated by the high-frequency voltage signal, the high-frequency voltage is injected only along the $\hat{d}^r$ -axis, as expressed in[23]

$$\begin{bmatrix} v^e_{\tilde{d}sh} \\ v^e_{\tilde{q}sh} \end{bmatrix} = \begin{bmatrix} V_{inj}\cos\omega_h t \\ 0 \end{bmatrix}. \tag{29}$$

When the rotor estimation angle error is negligible, $\cos 2\tilde{\theta}_r \approx 1$ and $\sin 2\tilde{\theta}_r \approx 2\tilde{\theta}_r$. According to Eq. (29), Eq. (28) can be simplified and expressed as

$$\begin{bmatrix} i^e_{\tilde{d}sh} \\ i^e_{\tilde{q}sh} \end{bmatrix} \approx \frac{V_{inj}\cos\omega_h t}{-\omega_h^2 L_{dh} L_{qh}} \begin{bmatrix} L_{qh} \\ (L_{qh} - L_{dh})\tilde{\theta}_r \end{bmatrix}. \tag{30}$$

On the basis of the first row of Eq. (30), the resulting high-frequency current along the $\hat{d}^r$ -axis can be expressed as

$$i^e_{\tilde{d}sh} = I^e_{\tilde{d}sh}\cos\omega_h t\,, \tag{31}$$

where $I^e_{\tilde{d}sh} = V_{inj} \big/ (-\omega_h^2 L_{dh})$ is the amplitude of the high-frequency current along the $\hat{d}^r$ -axis. By considering the high-frequency current amplitude, inductance parameters, and the selected injection frequency, the amplitude of the injected high-frequency voltage can be determined. Furthermore, on the basis of the second row of Eqs. (30) and (31), the resulting high-frequency current along the $\hat{q}^r$ -axis can be expressed as

$$i^e_{\tilde{q}sh} = \frac{(L_{qh} - L_{dh})\tilde{\theta}_r}{L_{qh}} i^e_{\tilde{d}sh}\,. \tag{32}$$

Referring to Eq. (32), the estimation error of the rotor angle can be expressed as

$$\tilde{\theta}_r = \frac{L_{qh}}{L_{qh} - L_{dh}} \frac{i^e_{\tilde{q}sh}}{i^e_{\tilde{d}sh}}\,. \tag{33}$$

When a high-frequency voltage signal is injected along the $\hat{d}^r$ -axis, the measured high-frequency currents along the $\hat{d}^r$ - and $\hat{q}^r$ -axes are processed through synchronization. From Eq. (33), the calculated rotor angle estimation error can be expressed as

$$\Delta\theta_r = \frac{L_{qh}}{L_{qh} - L_{dh}} \frac{i^e_{\tilde{q}sh}}{i^e_{\tilde{d}sh}}\,. \tag{34}$$

Accordingly, the calculated rotor angle estimation error ($\Delta\theta_r$) corresponds to the actual rotor angle estimation error ($\tilde{\theta}_r$). The current rotor estimation angle is updated by adding the calculated rotor angle estimation error to the previous rotor estimation angle, as

$$\hat{\theta}_r(k) = \theta_r(k-1) + \Delta\theta_r(k). \tag{35}$$

The estimated rotor speed can be expressed as

$$\hat{\omega}_r = (\omega_r(k) - \omega_r(k-1))/T_s, \tag{36}$$

where T_s is the sampling time for the estimated rotor speed.

Figure 2 illustrates the rotor position estimation mechanism based on the proposed high-frequency signal injection technique. Here, $3 \Rightarrow 2^e$ represents the coordinate transformation from the three-phase system to the two-axis synchronous reference frame, *BPF* represents the bandpass filter, and Z^{-1} represents the unit delay.

Figure 3 illustrates the block diagram of the proposed speed estimation FOC IPMSM drive using the high-frequency signal injection technique. This system includes a speed controller; d^e-axis and q^e-axis stator current controllers; d^e-axis and q^e-axis decoupled calculations; d^e-axis high-frequency voltage injection; i^{e*}_{qs}- calculation; coordinate transformation between the three-phase system and the two-axis synchronous reference frame ($2^e \Leftarrow 3$, $2^e \Rightarrow 3$); and the rotor position estimation. In this system, the speed, and d^e-axis and q^e-axis stator current controllers were designed by the pole placement method. The rotor position estimation mechanism based on the high-frequency signal injection technique was considered. Furthermore, the three-phase stator currents (i_{as}, i_{bs}, and i_{cs}) were measured from the IPMSM using electromagnetic Hall effect current sensors.

5. Simulation Setup and Results

A three-phase, 220 V, 0.75 kW, Y-connected IPMSM was used as the controlled plant in the experiments to validate the effectiveness of the proposed speed estimation FOC IPMSM drive

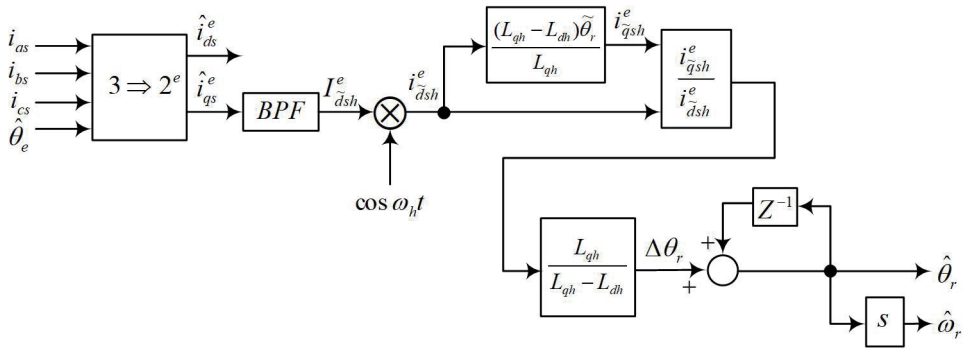

Fig. 2. (Color online) Rotor position estimation based on high frequency signal injection.

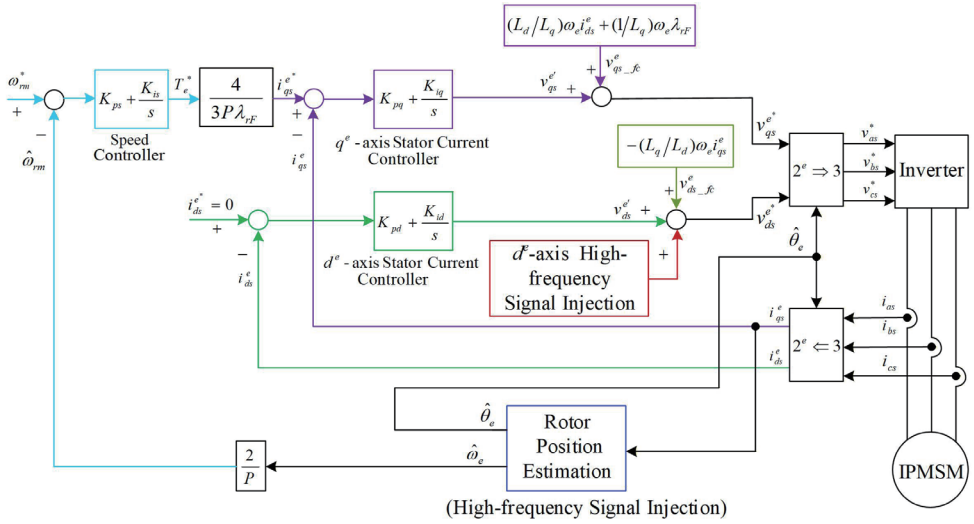

Fig. 3. (Color online) Speed estimation FOC IPMSM drive using high-frequency signal injection technique.

using the high-frequency signal injection technique. In a running cycle, the speed command was designed as follows: forward acceleration from $t = 0$ to $t = 1$ s, forward steady-state running for $1 \le t \le 3$ s, forward braking to reach zero speed within the interval from $3 \le t \le 4$ s, reverse acceleration from $t = 4$ s to $t = 5$ s, reverse steady-state running for $5 \le t \le 7$ s, and reverse braking to reach zero speed within the interval from $7 \le t \le 8$ s.

The simulated and experimental responses of the proposed speed estimation FOC IPMSM drive using the high-frequency signal injection technique under a 2 N·m load and a reversible steady-state speed command of 30 rev/min are shown in Figs. 4 and 5 for the first three running cycles. Figures 4 and 5 each contains six plots: (a) command (dashed line) and estimated (solid line) rotor speed; (b) command (dashed line) and actual (solid) rotor speed; (c) q^e-axis stator current; (d) electromagnetic torque; (e) estimated synchronous position angle; and (f) estimated stator flux locus.

According to the simulated and experimental responses during reversible transient and steady-state operations, the proposed high-frequency signal injection technique accurately estimates the rotor speed. The q^e-axis stator current and electromagnetic torque confirm the loading effect. The sawtooth waveform of the estimated synchronous position angle and the circular trajectory of the estimated stator flux locus validate the correctness of the coordinate transformation between the synchronous and stationary reference frames. Hence, the developed speed estimation FOC IPMSM drive using the high-frequency signal injection technique has demonstrated that the desired performance can be achieved.

6. Conclusions

A high-frequency signal injection technique was developed for a speed estimation FOC IPMSM drive. The decoupled FOC IPMSM drive based on stator current and stator flux

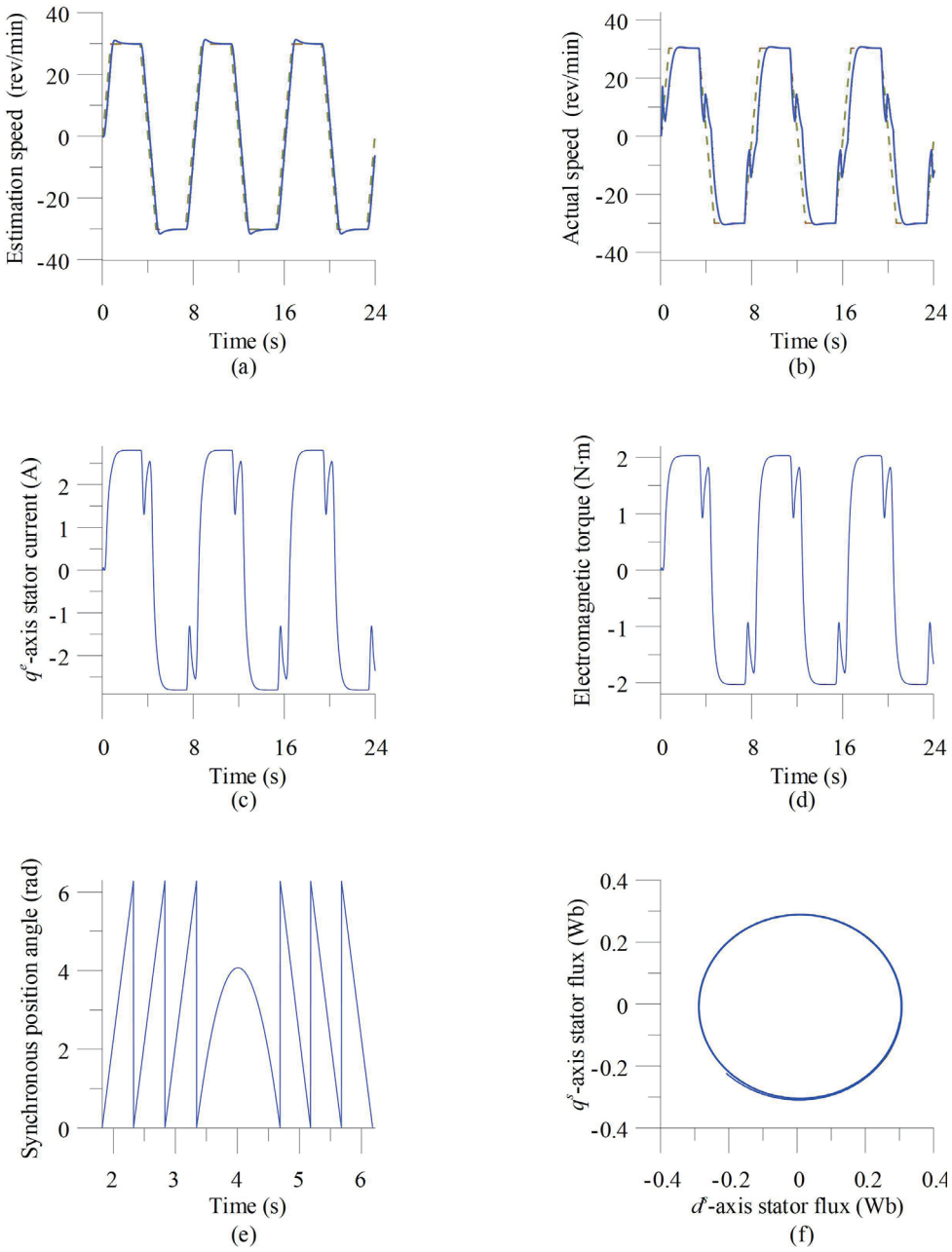

Fig. 4. (Color online) Simulated responses of the proposed speed estimated FOC IPMSM drive using high-frequency signal injection technique under a 2 N·m load and a reversible steady-state speed command of 30 rev/min: (a) estimated rotor speed, (b) actual rotor speed, (c) q^e-axis stator current, (d) electromagnetic torque, (e) estimated synchronous position angle, and (f) estimated stator flux locus (q^s-axis vs d^s-axis).

information was established. The speed, d^e-axis stator current, and q^e-axis stator current controllers were designed by the pole placement method. Rotor speed estimation was achieved through high-frequency signal injection. Three-phase stator current measurements for implementing the speed estimation FOC IPMSM drive were provided by Hall effect current

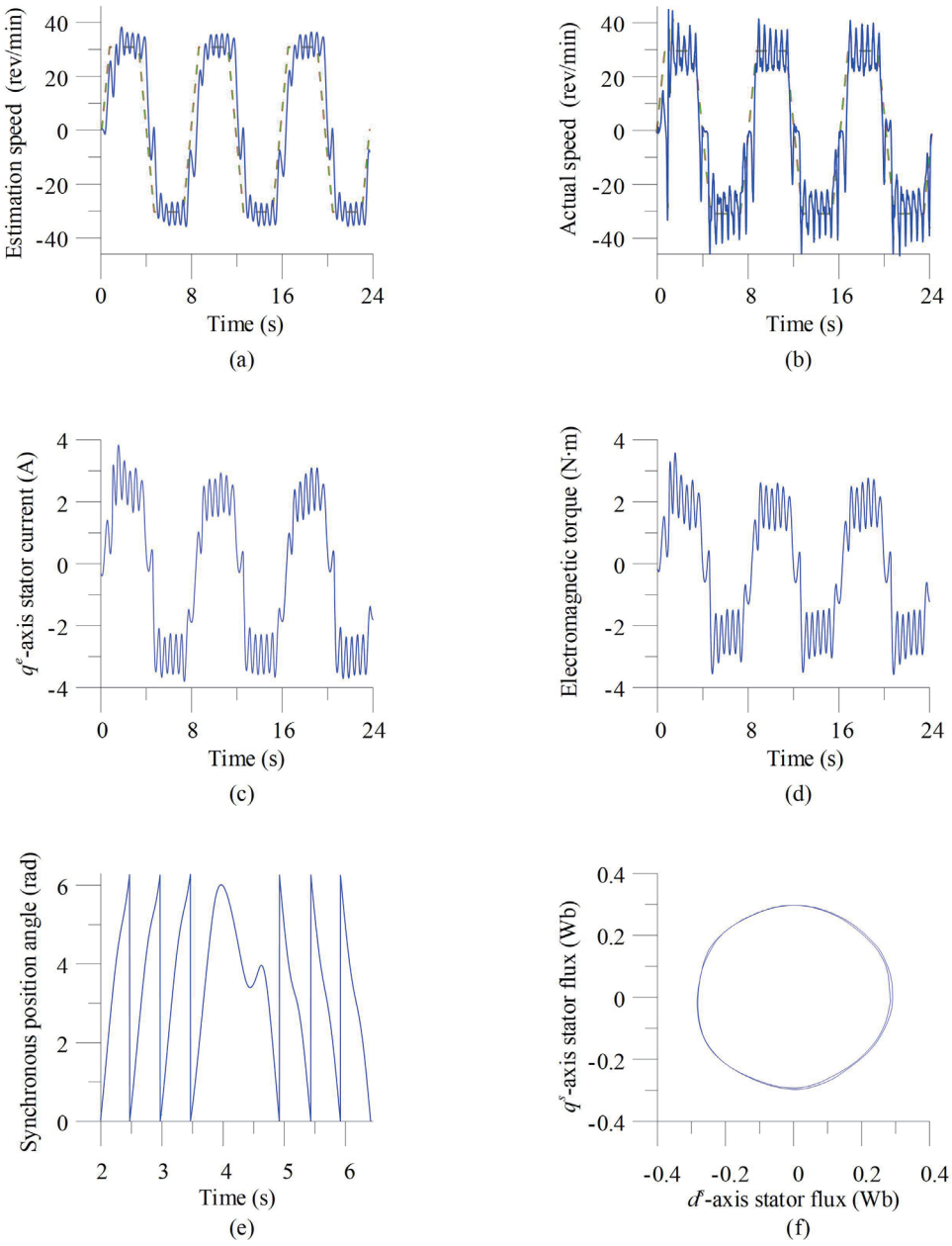

Fig. 5. (Color online) Experimental responses of the proposed speed estimated FOC IPMSM drive using high-frequency signal injection under a 2 N·m load and a reversible steady-state speed command of 30 rev/min: (a) estimated rotor speed, (b) actual rotor speed, (c) q^e-axis stator current, (d) electromagnetic torque, (e) estimated synchronous position angle, and (f) estimated stator flux locus (q^s-axis vs d^s-axis).

sensors. Simulation and experimental responses for reversible steady-state speed commands under load conditions confirmed the promising performance of the proposed speed estimation FOC IPMSM drive using the high-frequency signal injection technique.

Acknowledgments

This study was supported by the National Science and Technology Council of Taiwan under contract number NSTC 113-2637-E-167-003 (duration: August 1, 2024–July 31, 2025).

References

1 Y. C. Luo, W. C. Lin, H. O. Huang, and W. C. Pu: Sens. Mater. **37** (2025) 1181. https://doi.org/10.18494/SAM.5219
2 X. Wang, D. Luo, and D. Xiao: IEEE Trans. Power Electron. **40** (2025) 6519. https://doi.org/TPEL.2024.3524793
3 Y. Liu, M. Lu, W. Jiang, and W. Zhang: IEEE J. Emerging. Sel. Top. Power Electron. **12** (2024) 2017. https://doi.org/10.1109/JESTPE.2024.3357505
4 A. M. Aljehaimi and P. Pillay: IEEE Trans. Ind. Appl. **54** (2018) 2319. https://doi.org/10.1109/TIA.2018.2794338
5 S. Wan, H. Wang, Y. Zuo, G. Guo, and X. Ge: CPSS Trans. Power Electron. Appl. **9** (2024) 454. https://doi.org/10.24295/CPSSTPEA.2024.00025
6 X. Wu, T. Wu, S. Huang, W. Pan, M. Lyu, Y. He, and H. Cui: IEEE Trans. Power Electron. **37** (2022) 7916. https://doi.org/10.1109/TPEL.2022.3151769
7 G. Foo and M. F. Rahman: IEEE Trans. Ind. Electron. **57** (2010) 395. https://doi.org/10.1109/TIE.2009.2030815
8 G. Wang, T. Li, G. Zhang, X. Gui, and D. Xu: IEEE Trans. Ind. Electron. **61** (2014) 5115. https://doi.org/10.1109/TIE.2013.2264791
9 X. Wu, D. Yang, X. Yu, K. Lu, T. Wu, S. Huang, and H. Cui: IEEE Trans. Ind. Electron. **38** (2023) 10128. https://doi.org/10.1109/TPEL.2023.3280254
10 M. Morawiec, A. Lewicki, and I. C. Odeh: IEEE Trans. Ind. Electron. **71** (2024) 1399. https://doi.org/10.1109/TIE.2023.3250851
11 Y. Mei, K. Sun, and Y. Shi: Chinese J. Elec. Eng. **1** (2015) 85. https://doi.org/10.23919/CJEE.2015.7933141
12 G. Zhang, G. Wang, D. Xu, and N. Zhao: IEEE Trans. Ind. Electron. **31** (2016) 1450. https://doi.org/10.1109/TPEL.2015.2424256
13 W. Zine, Z. Makni, E. Monmasson, L. Idkhajine, and B. Condamin: IEEE Trans. Ind. Inform. **14** (2018) 1942. https://doi.org/10.1109/TII.2017.2765398
14 F. J. Lin, Y. C. Hung, J. M. Chen, and C. M. Yeh: IEEE Trans. Ind. Inform. **10** (2014) 1226. https://doi.org/10.1109/TII.2014.2305591
15 X. Wu, C. Wang, M. Lyu, W. Liao, X. Yu, T. Wu, S. Huang, and H. Cui: IEEE Trans. Ind. Electron. **70** (2023) 11044. https://doi.org/10.1109/TIE.2022.3229368
16 G. Zhang, Y. Yan, Q. Wang, D. Ding, G. Wang, L. Ding, Y. Li, and D. Xu: IEEE Trans. Power Electron. **39** (2024) 6136. https://doi.org/10.1109/TPEL.2024.3365735
17 Y. Shi, K. Sun, L. Huang, and Y. Li: IEEE Trans. Ind. Electron. **59** (2012) 4169. https://doi.org/10.1109/TIE.2011.2168792
18 F. Mwasilu and J. W. Jung: IEEE Trans. Power Electron. **31** (2016) 5746. https://doi.org/10.1109/TPEL.2015.2495240
19 G. H. B. Foo, X. Zhang, and D. M. Vilathgamuwa: IEEE Trans. Ind. Electron. **60** (2013) 3485. https://doi.org/10.1109/TIE.2013.2244537
20 C. H. Liu: Control of AC Electrical Machines (Tunghua, Taipei, 2008) 4th ed., Chap. 6 (in Chinese).
21 E. Al-nabi, B. Wu, N. R. Zargari, and V. Sood: IEEE Trans. Ind. Electron. **60** (2013) 1711. https://doi.org/10.1109/TIE.2012.2191752
22 Y. Jeong, R. D. Lorenz, T. M. Jahns, and S. Sul: IEEE Trans. Ind. Appl. **41** (2005) 38. https://doi.org/10.1109/TIA.2004.840978
23 J. Zhang, G. Liu, and Q. Chen: IEEE Trans. Transp. Electrif. **7** (2021) 1516. https://doi.org/10.1109/TTE.2020.3048582